

Size dependence of complex refractive index function of growing nanoparticles

A. Eremin · E. Gurentsov · E. Popova · K. Priemchenko

Received: 14 September 2010 / Revised version: 30 November 2010 / Published online: 15 February 2011
© Springer-Verlag 2011

Abstract The evidence of the change of the complex refractive index function $E(m)$ of carbon and iron nanoparticles as a function of their size was found from two-color time-resolved laser-induced incandescence (TiRe-LII) measurements. Growing carbon particles were observed from acetylene pyrolysis behind a shock wave and iron particles were synthesized by pulse Kr–F excimer laser photodissociation of $\text{Fe}(\text{CO})_5$. The magnitudes of refractive index function were found through the fitting of two independently measured values of particle heat up temperature, determined by two-color pyrometry and from the known energy of the laser pulse and the $E(m)$ variation. Small carbon particles of about 1–14 nm in diameter had a low value of $E(m) \sim 0.05\text{--}0.07$, which tends to increase up to a value of 0.2–0.25 during particle growth up to 20 nm. Similar behavior for iron particles resulted in $E(m)$ rise from ~ 0.1 for particles 1–3 nm in diameter up to ~ 0.2 for particles > 12 nm in diameter.

1 Introduction

The method of laser-induced incandescence (LII) is extensively used for soot particles size and volume fraction measurements in combustion [1–4]. Generally, soot is comprised of spheroid carbonaceous particles with sizes of about 5–50 nm, coupled together to form fractal-like aggregates [5]. However, typical primary soot particles sizes measured by LII are in a more narrow range—20–40 nm, because of

extremely short (practically unresolved) soot growing zones in combustion processes [6]. Therefore all particle properties are commonly related to particles which have grown up to their final size. However, properties of growing nanoparticles could essentially be size dependent. For example, calculations predict a melting point size dependence of different nanoparticles [7–9]. There are also observations of enhancement of heat capacity of small nanoparticles [10]. Therefore one can expect that the optical properties of nanoparticle could be size dependent as well. Practically all methods of nanoparticle monitoring (scattering, extinction, laser-induced incandescence, etc.) are based on the optical properties, which are represented by the complex refractive index of the particle material. The function $E(m)$, based on the value of complex refractive index, is used in LII models to account for the part of the laser energy absorbed by particles. So, reliable knowledge of the refractive index function of nanoparticles is of great importance for LII and others optical diagnostics. The dependence of the soot refractive index function on wavelength was discussed in a number of works (see for instance [11]). It is necessary to underline that almost all authors analyze the experimental data of LII measurements under the assumption that optical, and in some cases thermodynamic properties of registered particles are invariable (and as a rule, coincide with known properties of soot) both on different times of process of particle formation, and at different temperatures. In fact, the $E(m)$ size dependence of soot particles is poorly known and $E(m)$ of iron nanoparticles is not investigated at all. There are only some evidences of the change of carbon nanoparticle optical properties in dependence on their size, especially in the range from 1–2 to 10–20 nm [12–16]. Recently an increase of $E(m)$ by a factor of two was observed in a soot growing zone from the lowest to the highest heights of premixed one-dimensional ethylene/air flame [17]. So, it is clear that

A. Eremin · E. Gurentsov (✉) · E. Popova · K. Priemchenko
Joint Institute for High Temperature, Izorskaya st. 13(2),
125412 Moscow, Russia
e-mail: gurentsov@ihed.ras.ru
Fax: +7-495-4857990

the experimental investigations of the process of nanoparticle growth require knowledge of the behavior of the optical properties with size. Convenient means for observation of nanoparticle formation process are a shock tube reactor [18–20] and especially a pulse laser photolysis reactor [21, 22]. Varying the time delay between the start of particle formation and the moment of LII firing one may observe the different stages of nanoparticle growth.

The goal of this study was to get information about $E(m)$ size dependence of carbon and iron particles during their growth. We have adopted the methodology of [23] and applied it to the in-situ determination of $E(m)$ of carbon and iron nanoparticles formed in a shock tube and in a photolysis reactor. Comparison of LII theory and experimentally determined intensity decay curves resulted in determination of primary particle size.

2 Experimental

2.1 Nanoparticle synthesis

The soot particles were synthesized from the pyrolysis of 3% acetylene in argon behind a reflected shock wave in a diaphragm type shock tube with inner diameter 50 mm. Post-shock gas properties were determined based on measured shock wave velocity by applying one-dimensional gas-dynamic shock wave theory and assuming frozen reaction conditions. The temperature and pressure values given below are the “frozen” post-shock parameters, ranging from 1800 to 2100 K (in the region of maximum “soot yield” observed by extinction measurements) and 6–8 bars. Laser light extinction and TiRe-LII diagnostics were applied to follow carbon particle growth. The attenuation of CW He–Ne laser operated at wavelength 633 nm was measured by detector PDA10A-ES (THORLABS). By extinction measurements we have observed a rise of condensed phase volume fraction which flattens out at all investigated conditions before the time of 1600 μ s.

The iron nanoparticles were synthesized by the Kr–F excimer pulse laser photolysis of $\text{Fe}(\text{CO})_5$ at room temperature (details of experiments are given in [22]). One side opened quartz cell with volume of 1 cm^3 was used as the photolysis reactor. The evacuation and filling of the cell with prepared manometrically mixture of $\text{Fe}(\text{CO})_5$ (Fluka, 99%, used after degassing) and high-purity bath gases Ar, He, Xe (99.998%) were arranged by the flange connection glued on the opened end. For synthesis of the iron nanoparticles the mixtures contained 5, 11 and 20 mbar of $\text{Fe}(\text{CO})_5$ in 1 bar of He, Ar and Xe or undiluted 11 mbar $\text{Fe}(\text{CO})_5$ were used. One side of the cell (18 \times 8 mm) was fitted with the size of the central part of excimer laser (model ELI-91M) beam cross section to illuminate the whole inner volume. The laser energy from

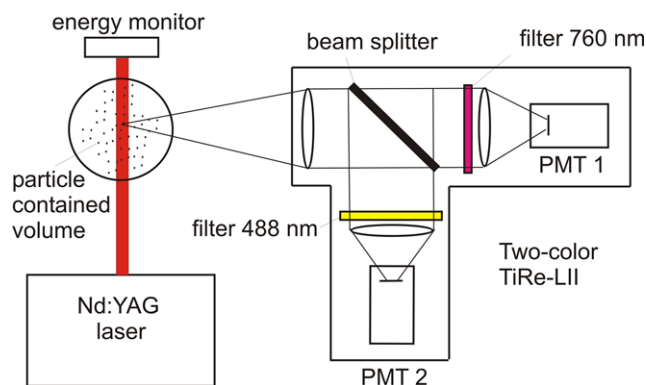


Fig. 1 Setup for LII measurements

one pulse experiment was measured through the evacuated cell before the experiment and through the cell filled with the mixture of $\text{Fe}(\text{CO})_5$ and bath gas. The incident laser energy density used in the experiments was in the range of 25–35 mJ/cm^2 with variation of about 5 mJ/cm^2 from pulse to pulse. With the assumption that two 248 nm photons absorbed by $\text{Fe}(\text{CO})_5$ molecules yield one Fe atom formation we have estimated the iron atom concentration generated after pulse photolysis. Immediately after appearance of the iron atoms in the reactor the particles start to grow. This process was observed by registration of laser light extinction during 100 ms reflecting the increase of volume fraction of condensed phase.

2.2 TiRe-LII diagnostics

In both types of experiments the same self-made apparatus for TiRe-LII measurements was used (Fig. 1). An Nd:Yag laser LQ-129 (SOLAR Laser Systems) operated at a wavelength of 1064 nm was applied for particle heat up. Maximum laser pulse energy at a wavelength 1064 nm was 500 mJ, pulse duration was 12 ns. The laser energy–time profile was measured using a retro-reflection of the beam from one of the optics, which was subsequently attenuated using neutral density filters and detected with a Hamamatsu H6780-20 photomultiplier module coupled to a LeCroy WaveRanner 6060A oscilloscope. This profile is presented on Fig. 2 and its half width is close to pulse duration declared by manufacturer. To get the laser energy spatial profile the laser beam was expanded by a lens up to 24 mm in diameter and energy values were scanned using a square aperture 1 \times 1 mm^2 in size, moving in horizontal and vertical directions. Measured energy values were annularly averaged to get an axisymmetric profile which is better-behaved for calculations. The averaged spatial profile is shown in Fig. 3. The laser fluence was varied in the range of 0.3–0.5 J/cm^2 . These fluences are higher than the so-called low fluence conditions ($<0.2 \text{ J}/\text{cm}^2$) [11], however at fluences below 0.3 J/cm^2 the LII signals from the particles could not be

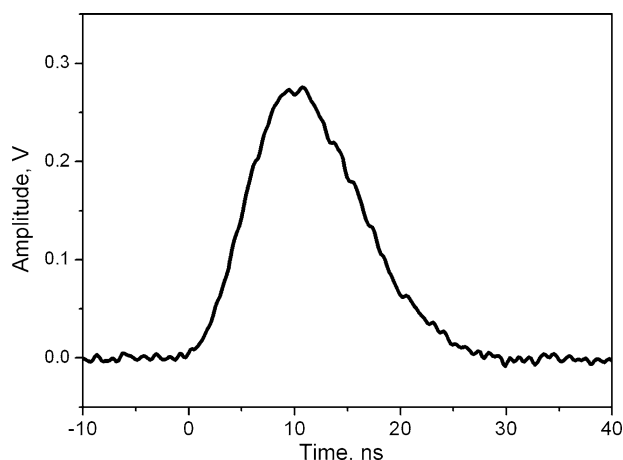


Fig. 2 Laser energy–time profile

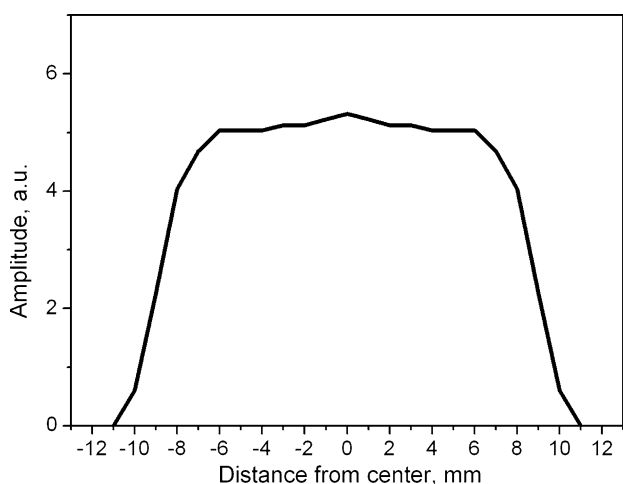


Fig. 3 Laser energy averaged axisymmetric spatial profile

observed. The incandescence signals registration was performed using Hamamatsu H6780-20 photomultiplier modules, two narrow band pass filters centered at wavelengths of 488 and 760 nm and a 500 MHz band pass scope LeCroy WaveRanner 6060A. The measurements of the maximum amplitude of laser-induced incandescence signals at two wavelengths were used for a particle determination of the heat up temperature.

TiRe-LII measurements of carbon particle sizes at different time delays from 200 up to 1600 μs after reflected shock arrival have been carried out. This time was restricted by the working period of the shock tube (arriving of rarefaction wave at the measurement cross section) which was not more than 1600 μs . To get the particle size-time profile several series of experiments with different delays at the same temperature and pressure were performed. The variation of frozen temperature in shock tube from shot to shot was in the range ± 15 K inside one series of experiments. The Yag laser beam passed in perpendicular direction to the shock

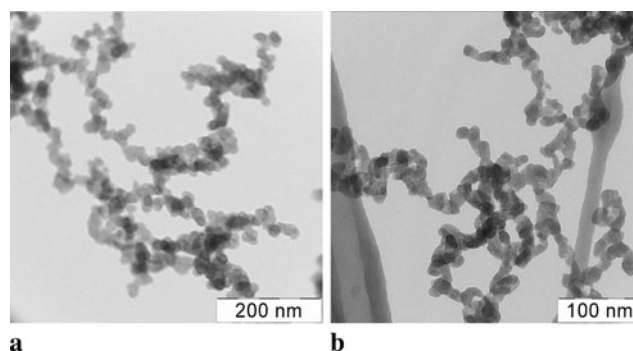


Fig. 4 Examples of TEM images of nanoparticles. **(a)** Carbon particles formed from shock tube pyrolysis of 3% C_2H_2 in argon at temperature 1950 K and pressure 7.2 bar; **(b)** iron particles synthesized from photolysis of 11 mbar $\text{Fe}(\text{CO})_5$ in 1 bar helium at room temperature

tube axis through two quartz windows. The registration of two-color LII radiation was performed through the quartz end plate of the shock tube installed at a distance of 45 mm from the windows.

TiRe-LII signals from iron particles were detected after a photo-dissociation pulse of the excimer laser in the time range from 5 up to 10000 μs to get the particle size-time profiles. Laser beam passed through the right-angled quartz cell in horizontal direction and LII registration was performed vertically through the upper side of the reactor.

2.3 TEM particle sizing

The final carbon particles were scraped from the glass end plate of the shock tube after the experiment and deposited on the copper TEM grids covered by carbon net without using of any solutions. After that the shock tube walls were cleaned several times by alcohol. The iron particles were collected in quartz reactor in separate experiments without running of Yag laser to avoid its influence on the structure of the particle (due to volume of the quartz cell being comparable with the volume illuminated by the laser beam). The copper TEM grids covered by carbon net were placed on the bottom of the reactor and particles deposited on the grid under natural gravity during 15 min after the pulse experiment. After that the quartz reactor was opened and cleaned by alcohol. Examples of TEM images of carbon and iron nanoparticles are presented on Fig. 4. More or less spherical primary particle agglomerates were found on all TEM images. Mostly the agglomerates have a structure like particle chains but sometimes more dense structures were observed. We suppose that the agglomerate structure depends on the way how the particle samples were prepared and what kinds of TEM parameters were used. For example, we observed that at the energy of an electron beam of about 100 kV the iron particle chains had moved and formed denser agglomerates. In our case we can conclude that in the gas phase carbon and iron particle agglomerates had a loose structure

like particle chains with an assumed point contact between the primary particles.

Log-normal particle-size distribution was used for TEM particle sizing:

$$df = \frac{1}{\sqrt{2\pi}d_p \ln \sigma} \exp \left[-\frac{(\ln d_p - \ln CMD)^2}{2(\ln \sigma)^2} \right] dd_p, \quad (1)$$

where d_p is the current primary particle diameter, CMD is the count median diameter and σ is the standard deviation. The iron and carbon nanoparticle sizing was carried out by approximation of histograms of size distribution measured using TEM micrographs by the log-normal function (1). The final carbon primary particle CMD of 15–17 nm with $\sigma = 1.1$ and iron particle CMD of 7–16 nm with $\sigma = 1.1$ –1.2 were found at the conditions investigated.

3 LII model

3.1 Energy and mass balance equations

The LII model used for particle-size evaluation considers the current particle temperature T_p during their heating and cooling by solution of the energy and mass balance equations (2), (3):

$$\frac{d(m_p c_p T_p)}{dt} = \dot{q}_{\text{abs}} - \dot{q}_{\text{rad}} - \dot{q}_{\text{cond}} - \dot{q}_{\text{evap}}, \quad (2)$$

$$\frac{dm_p}{dt} = -J_{\text{evap}}. \quad (3)$$

Here m_p and c_p are mass and heat capacity of nanoparticles, t is time, J_{evap} is the mass loss rate from the particle surface during evaporation process, \dot{q}_{abs} is the laser energy per unit time, absorbed by nanoparticle, \dot{q}_{evap} , \dot{q}_{rad} , \dot{q}_{cond} are the energy loss rates from nanoparticle in the processes of evaporation, thermal radiation and conductive heat transfer with the molecules of bath gas correspondingly.

During the laser heating of nanoparticle the heat capacity of its material is essentially changing, therefore in our model the temperature dependences of heat capacity for carbon and iron nanoparticle have been used. Due to the absence of reliable properties of iron and carbon particles we have used the properties of bulk iron and graphite [24]. These dependences are shown in Figs. 5 and 6. In the model a polynomial approximation for graphite was used:

$$c_p = a_{pp} + b_{pp}T_p + \frac{c_{pp}}{T_p^2}, \quad (4)$$

where a_{pp} , b_{pp} and c_{pp} are empirical coefficients. For iron nanoparticles the heat capacity of iron as the piecewise continuous function was used in the model (see Fig. 6).

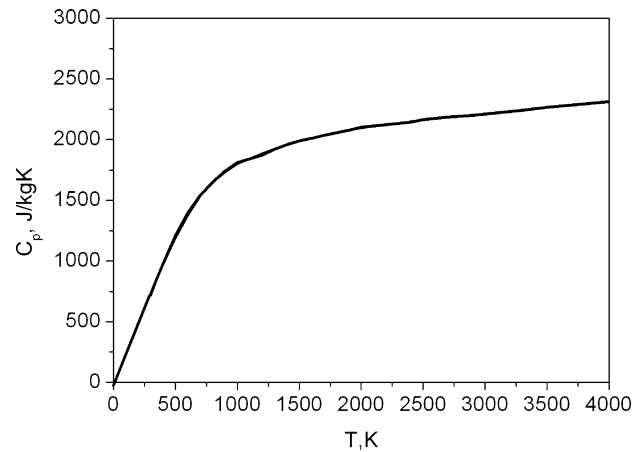


Fig. 5 The graphite heat capacity temperature dependence [24]

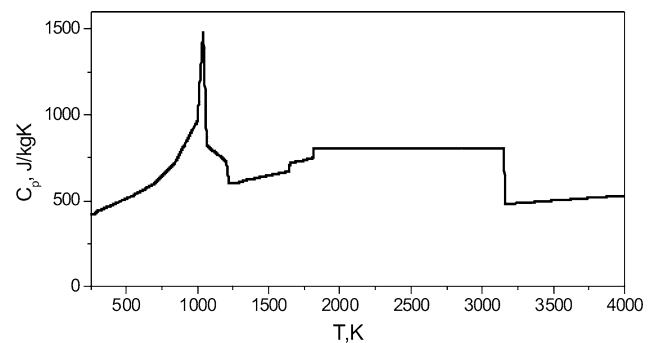


Fig. 6 The iron heat capacity temperature dependence [24]

The current particle mass in (2) was converted to current particle size by using a value of particle density. For the carbon particle, the temperature dependence of density for solid graphite $\rho = 2303.1 - 7.3106 \times 10^{-2}T$, reported in [5], was used. A simple linear approximation of the data for solid [25] and liquid [26] iron density $\rho = 8200 - 0.6T$ was adopted and used for iron nanoparticles. It is possible that the real density and heat capacity of the nanoparticle material could differ from the values for the bulk material. Therefore application of a particle density and heat capacity of bulk iron and graphite in the present analysis could lead to inaccuracy at the evaluation of the size dependence of the optical properties, which will be discussed below.

3.2 Laser energy absorption and refractive index function value determination

In the Rayleigh limit ($d_p \ll \lambda_{\text{laser}}$) the energy absorption by a nanoparticle with a diameter d_p can be written as [5]

$$\dot{q}_{\text{abs}} = \frac{\pi^2 d_p^3 E(m)}{\lambda_{\text{laser}}} g(t), \quad (5)$$

where $g(t)$ is the time profile of laser intensity given by the measured laser profile $g_m(t)$ (see Fig. 2) normalized and weighted by the laser fluence R_0 [J/m²]:

$$g(t) = \frac{R_0 g_m(t)}{\int_0^{60\text{ns}} g_m(t) dt}. \quad (6)$$

In (5) λ_{laser} is the wavelength of heat-up laser, $E(m)$ is a function of the complex refractive index $m = n - ik$ of the particle material:

$$E(m) = -\text{Im}\left(\frac{m^2 - 1}{m^2 + 1}\right) = \frac{6nk}{(n^2 - k^2 + 2)^2 + 4n^2k^2}. \quad (7)$$

Neglecting the heat losses by conductivity, evaporation and thermal radiation, the maximum nanoparticle heat-up temperature T_p^0 could be obtained by integration of (2) as

$$T_p^0 = T_g + \frac{6\pi \cdot R_0 \cdot E(m)}{\rho_p \cdot c_p \cdot \lambda_{\text{laser}}}. \quad (8)$$

Here ρ_p is nanoparticle density and T_g is the temperature of the surrounding gas. Usually the nanoparticle refractive index function $E(m)$ is unknown a priori, therefore to get the absolute T_p^0 value additional measurements are necessary. Two-color pyrometry of incandescence signals has been applied for T_p^0 measurements. For homogeneous laser energy spatial profile the value of T_p^0 could be determined from the ratio of two maximum amplitudes of LII signals registered at two different wavelengths in the visible spectrum [27]:

$$T_p^0 = \frac{hc}{k_B} \frac{\left(\frac{1}{\lambda_2} - \frac{1}{\lambda_1}\right)}{\ln\left[\frac{I_1}{I_2} \frac{I_{\text{TL}2}}{I_{\text{TL}1}} \frac{\varepsilon(\lambda_2)}{\varepsilon(\lambda_1)}\right] + \frac{hc}{k_B T_{\text{TL}}} \left(\frac{1}{\lambda_2} - \frac{1}{\lambda_1}\right)}, \quad (9)$$

where h , c , k_B are Planck constant, light velocity in vacuum, and Boltzmann constant, respectively, λ_1 and λ_2 are registered radiation wavelengths, I_1 and I_2 are maximum amplitudes of the registered LII signals, $I_{\text{TL}1}$, $I_{\text{TL}2}$, T_{TL} are the radiation intensities and the brightness temperature of the calibration tungsten strip lamp defined by manufactured pyrometer and tungsten spectral emissivity on the wavelengths λ_1 and λ_2 , ε_1 and ε_2 are nanoparticle spectral emissivity on wavelength λ_1 and λ_2 which in the Rayleigh limit are approximately inversely proportional to wavelength [5]:

$$\varepsilon(\lambda) = \frac{4\pi d_p E(m)}{\lambda}. \quad (10)$$

In this work spectral variations of $E(m)$ of carbon nanoparticles have been neglected in the visible spectral range 488–760 nm, where LII measurements were performed, according to [11]. The same assumption for iron particles was made, because of lack of knowledge about wavelength dependence of iron particle optical properties. For the non-homogeneous laser energy spatial profile (see Fig. 3), following [23] we have calculated the total thermal emission

intensity I_i^{cal} at the wavelengths λ_i by dividing the measured laser beam axisymmetric profile into K uniform segments:

$$I_i^{\text{cal}} = A \sum_{k=1}^K N \frac{\frac{2\pi c^2 h}{\lambda_i^5}}{\exp\left(\frac{hc}{\lambda_i k_B T_k}\right) - 1} \times \frac{\pi^2 d_p^3 E(m)_i}{\lambda_i} \Delta x, \quad (11)$$

where A is the cross section of the laser beam and N is the number of primary particles inside each segment of width Δx . The particle temperature inside the k th segment T_k corresponds to the (8). The theoretical effective particle temperature T_e could be determined from the expression for two-color pyrometry [23]:

$$\frac{I_1^{\text{cal}}}{I_2^{\text{cal}}} = \frac{E(m)_1 \lambda_2^6 \exp(hc/k_B \lambda_2 T_e) - 1}{E(m)_2 \lambda_1^6 \exp(hc/k_B \lambda_1 T_e) - 1}. \quad (12)$$

Substitution of (11) into (12), assuming $\exp(hc/k_B \lambda T) \gg 1$ leads to [23]

$$T_e = \frac{\frac{hc}{k_B} \left(\frac{1}{\lambda_2} - \frac{1}{\lambda_1}\right)}{\ln\left(\frac{\sum_{k=1}^K \exp\left(-\frac{hc}{k_B \lambda_1 T_k}\right)}{\sum_{k=1}^K \exp\left(-\frac{hc}{k_B \lambda_2 T_k}\right)}\right)}. \quad (13)$$

Finally, the value of $E(m)$ was adjusted until (9) is equal to (13).

3.3 Energy loss by heat conductivity with bath gas

The main energy loss during particle cooling in our experiments proceeds in free molecular conditions of particle heat transfer with inert surrounding gas [28]:

$$\dot{q}_{\text{cond}} = \alpha \pi d_p^2 \frac{P}{2} \sqrt{\frac{8k_B T_g}{\pi \mu_g}} \left(\frac{\gamma + 1}{\gamma - 1}\right) \left(\frac{T_p(t)}{T_g} - 1\right). \quad (14)$$

In this equation T_g is the temperature of the surrounding gas, k_B is the Boltzmann constant, α is the thermal energy accommodation coefficient of the gas molecules with the particle surface, μ_g is the molar mass of the bath gas molecules, P is the pressure of the gas, γ is the ratio of the heat capacities of the gas. Most of the uncertainty in (14) comes from the accommodation coefficient, which is chosen from the known data in the literature, or it is the model parameter. In present calculations for carbon nanoparticles in argon the value of $\alpha = 0.23$ [29] and for iron nanoparticles $\alpha = 0.1$ in argon and $\alpha = 0.01$ in helium [22] have been chosen.

3.4 Energy loss by particle evaporation

In the LII model heat losses by the particle evaporation are taken into account. It is supposed that the main evaporated species for carbon nanoparticle are C₃ clusters [29] and for

iron nanoparticles are iron atoms. The evaporation energy flux is defined as [30]

$$\dot{q}_{\text{evap}} = -\frac{\Delta H_V^\circ}{W_V} \frac{dm_p}{dt}, \quad (15)$$

where W_V is the molar mass of evaporated species, dm_p/dt is the rate of mass loss and ΔH_V° is the enthalpy of evaporation of particle material. Due to absence of reliable data for nanoparticles, the evaporation enthalpy of graphite, 7.9078×10^5 J/mol [31], and bulk iron, 3.7576×10^5 J/mol [27], were used. It is postulated that the evaporated species are in equilibrium with the particle surface and the vapor temperature is equal to the particle temperature. Then the rate of mass loss could be defined as [30]

$$\frac{dm_p}{dt} = -\pi d_p^2 p_V \sqrt{\frac{W_V}{2\pi R T_p}}, \quad (16)$$

where R is the universal gas constant. The vapor pressure p_V above the particle surface is calculated by the Clausius–Clapeyron equation:

$$p_V = p_{\text{ref}} \cdot \exp\left(-\frac{\Delta H_V^\circ}{R} \left(\frac{1}{T_p} - \frac{1}{T_{\text{ref}}}\right)\right), \quad (17)$$

where p_{ref} and T_{ref} are the pressure and temperature at the reference point on evaporation curve. For determination of vapor pressure of C₃ the graphite data $p_{\text{ref}} = 1$ bar and $T_{\text{ref}} = 3915$ K [31] were used. For iron atoms $p_{\text{ref}} = 3337$ Pa and $T_{\text{ref}} = 2500$ K [27] were implemented. In our experiments the carbon particle peak temperature measured by two-color pyrometry was found to be in the range of 2900–3400 K. These temperatures are less than the graphite sublimation threshold (around 4000 K). When modeling the LII signal the contribution of evaporation was found to be negligible. The iron particle maximum heat up temperature measured in the range 2100–2500 K was also lower than the evaporation temperature of iron (around 3100 K). So in both cases the LII model does not show any essential evaporation heat and mass loss during particle heating and after that. It makes our assumption realistic about neglecting of evaporation during particle heating up to the temperature T_p^0 when $E(m)$ measurements were carried out (see (8)).

3.5 Energy loss by heat radiation

For the radiation heat loss from the particle surface in all spectra range the Stephan–Boltzmann law is used:

$$\dot{q}_{\text{rad}} = \pi d_p^2 \varepsilon \sigma_{\text{SB}} (T_p^4 - T_g^4), \quad (18)$$

where σ_{SB} is Stephan–Boltzmann constant, ε is the total emissivity, which was taken equal to 1. Though the real nanoparticle radiation differs from the black body one,

the uncertainty of heat loss determination near atmospheric pressure and $T_p < 4000$ K is negligible due to the very low radiation flux in comparison with heat conduction and evaporation.

3.6 LII signal calculation

The intensity of incandescence on the detected wavelength from single spherical particle with known temperature determined from the energy and mass balance equations in the processes of heating and cooling (2), (3) is calculated using Planck's law [32, 33]:

$$S_d(t) = C \cdot \left[\frac{d_p^3}{\exp(\frac{\chi \cdot T_g}{T_p(t)}) - 1} - \frac{d_{p0}^3}{\exp(\chi) - 1} \right]. \quad (19)$$

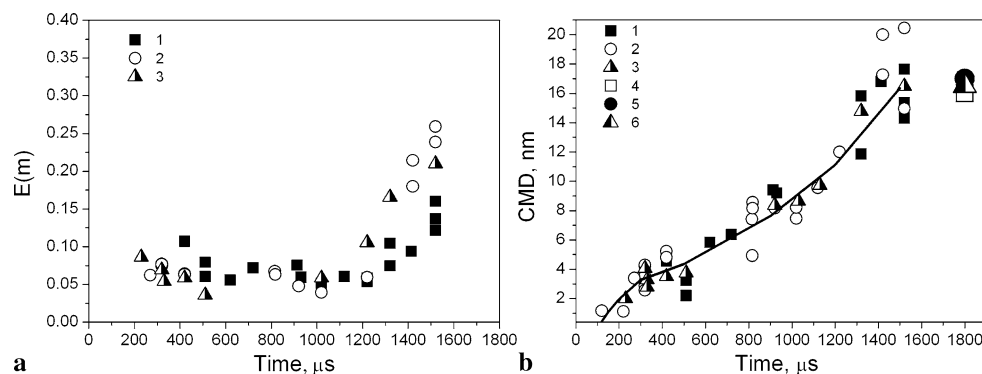
Here C is the instrument constant, $\chi = \frac{hc}{\lambda k_B T_g}$, d_{p0} is the initial particle diameter before the evaporation process. The above equation is relevant for a particle ensemble of uniform size d_{p0} .

The total radiation intensity from particle ensemble is calculated accounting for the nanoparticle log–normal size distribution function d_f (see (1)):

$$S(t) = n_p V_p \int_{d_{p01}}^{d_{p02}} S_d(t) f(d_{p0}) dd_{p0}. \quad (20)$$

The properties V_p and n_p are the irradiated volume and the number of particles per cm³ in that volume, respectively. The procedure of the calculation of TiRe-LII signal consisted of a number of iterations. After $E(m)$ determination described in Sect. 3.2, the first d_{p0i} (corresponding to the range of 1–100 nm with step of 0.1 nm) and σ values have been set. The particle temperature (corresponding to d_{p0i}) as a function of time was calculated based on the numerical solution of the differential equation system (2), (3), by using a second order Runge–Kutta method. At this step the laser energy time profile and time dependent particle properties were introduced. A current changing of d_{p0i} due to evaporation mass loss represented by d_{pi} was determined from (16). The above calculations were performed for different sectors of the laser beam as was done for the $E(m)$ determination and an effective time behavior of T_{ei} (13) was found. This temperature was used for calculation of the intensity of incandescence on the detected wavelength from single spherical particle (19). After that we have integrated (20) by equating of values of d_{p0i} with CMD in the log–normal distribution function (1). The resulting theoretical LII curve we have normalized and compared with normalized experimental TiRe-LII signal. The measured TiRe-LII signal was fitted by calculated curves obtained as was described above by variation of CMD and σ . Least square deviations between theoretical LII curve and experimental TiRe-LII signal as a

Fig. 7 The results of LII measurements of growing carbon particles during acetylene pyrolysis at different temperatures. **(a)** Particle refractive index function in dependence on reaction time; **(b)** particle sizes measured by LII and final particle sizes obtained by TEM. Symbols: 1, 2, 3 LII measurements at temperatures of 1850, 1950 and 2050 K; 4, 5, 6 corresponding results of TEM sizing; a line is a best fit of the experimental data



function of CMD and σ were analyzed. On the field of possible solutions the best one was found as a valley of minimum values with a gradient toward a single minimum which is reached at two input parameters. The values of σ , obtained at all experimental conditions were in agreement with results of TEM analysis of final carbon and iron particle-size distribution.

4 Results and discussion

4.1 Growing carbon particles

Two-color LII measurements of growing carbon particles had been carried out during acetylene pyrolysis behind a reflected shock wave at various temperatures. According to the procedure described above (see Sect. 3.2), the fitting of maximum heat up particle temperature with the same value calculated by use of absorbed laser energy resulted in a current value of particle refractive index function $E(m)$. Analysis of the time profiles of the intensity of the particle incandescence provided the current values of particle sizes (see Sect. 3.6). LII measurements of carbon particle size were performed at different time delays (from 200 to 1600 μ s) after the shock wave propagation. In Fig. 7 the carbon particle refractive index function $E(m)$ and size-time profiles measured at three various gas temperatures of 1850, 1950 and 2050 K are presented. From Fig. 7a one can see that at early times $E(m)$ has very low values (<0.1), and to ~ 1600 μ s it increases up to the values of 0.13–0.25 in dependence on experimental conditions. The large difference in $E(m)$ values in the latest times could be caused by increasing of uncertainties in model parameters with reaction time. TiRe-LII measurements of particle sizes showed (see Fig. 7b) that particles start to grow after some delay after shock wave arrival and then the process proceeds in a quite similar way at all measured temperatures. The smallest particle sizes measured by LII are about 1–2 nm and during 1600 μ s they grow up to 14–20 nm. The latest values of measured sizes show

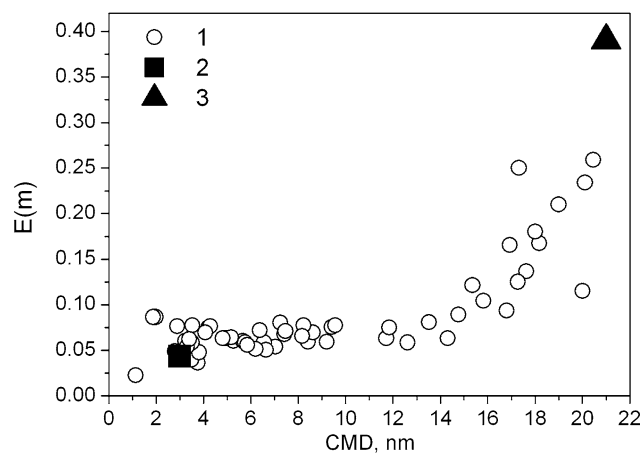


Fig. 8 The size dependence of refractive index function $E(m)$ of growing carbon particles at a wavelength of 1064 nm. 1 this work, 2 data [34], 3 results of $E(m)$ measurements of usual soot [23]

a reasonable agreement with the data of TEM analysis of final particle size, presented in the same plot. These results were used to obtain the size dependence of refractive index function at wavelength 1064 nm. This dependence is shown in Fig. 8. Besides our data in this plot the values of refractive index function of soot particles taken from the works [23] and [34] are presented. In [23] the values of $E(m)$ for the usual mature soot in a coflow laminar ethylene diffusion flame were derived. Assuming a wavelength independence of $E(m)$ and linear variation of $E(m)$ with wavelength, the derived values at 1064 nm were found; respectively, 0.395 and 0.42. In [34] the visible-transparent and sootlike structures were investigated in rich, premixed, ethylene/air flames. The refractive index for visible-transparent particles of 2–3 nm in size was determined on a wavelength of 266 nm from their absorption and fluorescence spectral behaviors and it was established to be $m = 1.4 - i0.08$, which corresponds to an $E(m)$ value of 0.043. Empty symbols in Fig. 8 represent our data of refractive index function values of growing carbon particles. For particle sizes from 2 up to 14 nm the behavior of the refractive index function was found to be nearly constant, about 0.05–0.07. These

Fig. 9 Approximation of normalized experimental LII time-resolved signals from carbon nanoparticles (*noisy curves*) by calculated curves (*solid lines*) at different values of $E(m)$. **(a)** Presumed common soot value of $E(m) = 0.35$, $CMD = 12.5$ nm; **(b)** extracted value of $E(m) = 0.067$, $CMD = 5.2$ nm

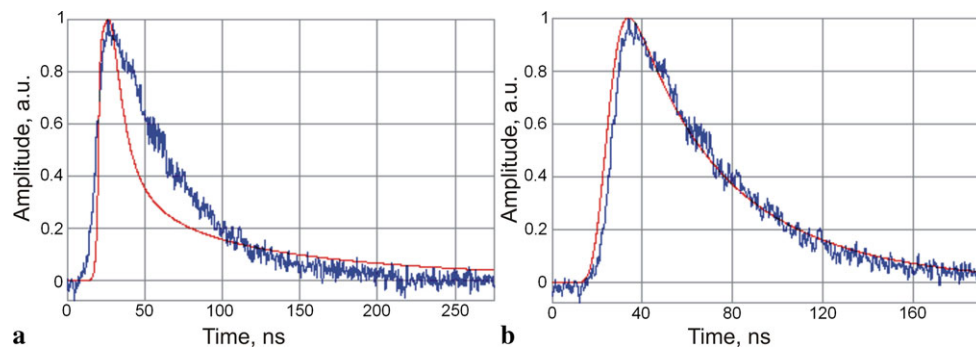
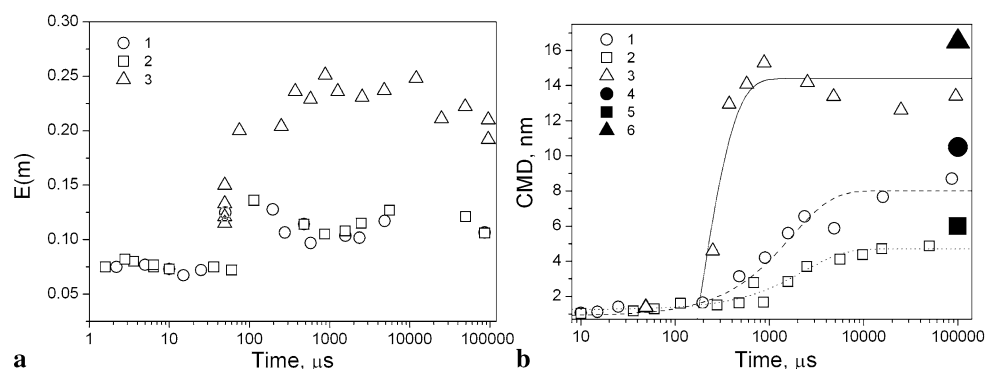


Fig. 10 The results of LII measurements of growing iron particles synthesized from $\text{Fe}(\text{CO})_5$ photolysis. **(a)** Growing particle refractive index function; **(b)** particle sizes measured by LII. Symbols: 1, 2, 3 measurements in the mixtures of 10 mbar $\text{Fe}(\text{CO})_5$ with 1 bar of Ar, He and without bath gas; 4, 5, 6 corresponding TEM data. Lines are best fits of the experimental points



low $E(m)$ values have a good agreement with the results reported in [34]. For particle sizes higher than 14 nm the $E(m)$ shows a sharp rise and tends to the usual soot values of 0.35–0.4 [11, 23], which correspond to particle sizes of 20–30 nm. It should be emphasized that the presented low value of the refractive index function for small particles corresponds to the best LII signal approximation, while the common soot value 0.35 set into the LII model leads to worse approximation and to oversized count median diameter due to a higher calculated particle heat up temperature (see Fig. 9).

4.2 Growing iron particles

In Fig. 10 the results of LII measurements of $E(m)$ and CMD of growing iron particles formed in the laser pulse photolysis experiments are presented. The iron particle refractive index functions and size-time profiles were obtained for different bath gases. The behavior of these data in various conditions carries kinetic information about the condensation of supersaturated iron vapor at room temperature. The dependence of $E(m)$ on reaction time (see Fig. 10a) shows a sharp rise at about 100 μs which could be explained by the abrupt particle optical properties change. The iron particle size-time profiles obtained by LII measurements are presented on Fig. 10b together with the TEM analysis results. As one can see, the results of final particle TEM-sizing differ from that obtained by LII at latest times of particle formation. This discrepancy could be caused by the iron particle oxidation in air when the samples were taken out of

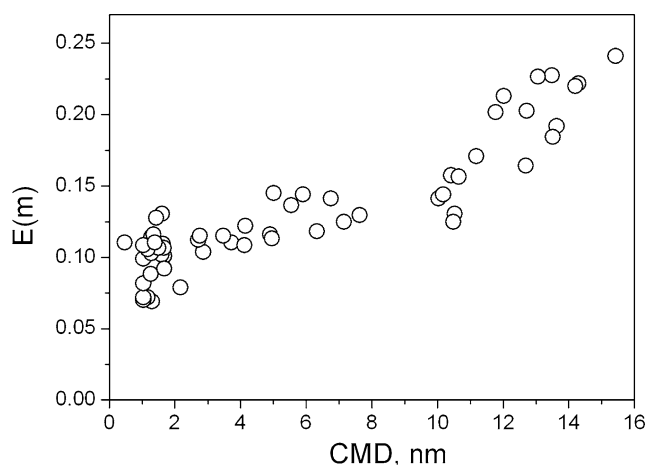


Fig. 11 The size dependence of the refractive index function $E(m)$ of growing iron particles at a wavelength of 1064 nm

the reactor. The electron micro-diffraction analysis showed that the samples totally consist of iron oxide, Fe_3O_4 , which could be a reason of increase of the particle size. Based on the data presented on Fig. 10 the size dependence of refractive index function for iron nanoparticles at the wavelength of 1064 nm has been found (see Fig. 11). One can see that this dependence is similar to that of carbon particles (see Fig. 8) and results in $E(m)$ rise from ~ 0.1 for particles 1–3 nm up to ~ 0.2 for particles > 12 nm in a diameter. Unfortunately no other data about iron particle refractive index function are available to compare to the results obtained. But

Fig. 12 Approximation of normalized experimental LII time-resolved signals from iron nanoparticles (*noisy curves*) by calculated curves (*solid lines*) at different values of $E(m)$.

(a) Presumed low value of $E(m) = 0.07$, $CMD = 1$ nm;
 (b) extracted value of $E(m) = 0.11$, $CMD = 2.5$ nm;
 (c) presumed high value of $E(m) = 0.16$, $CMD = 25$ nm

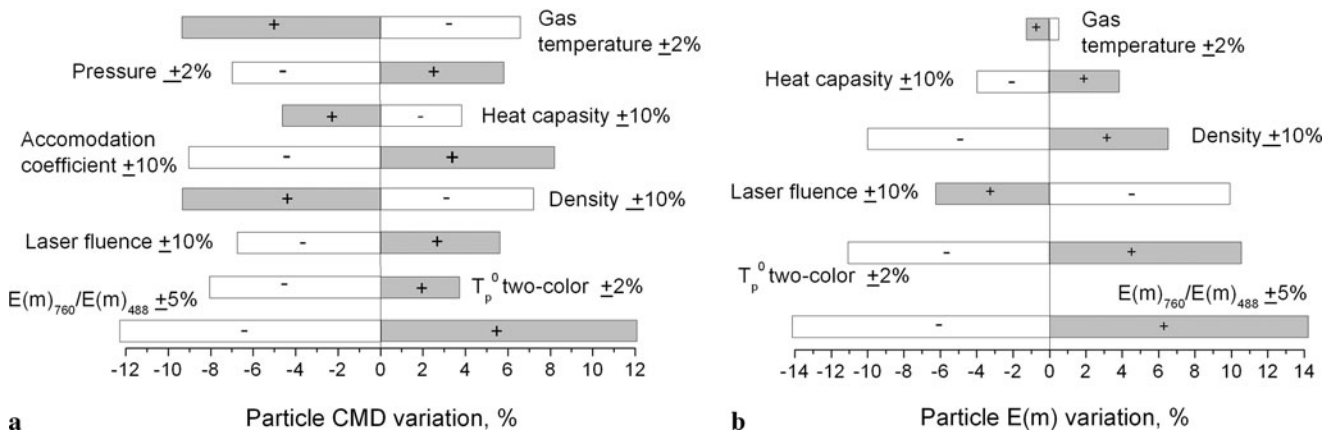
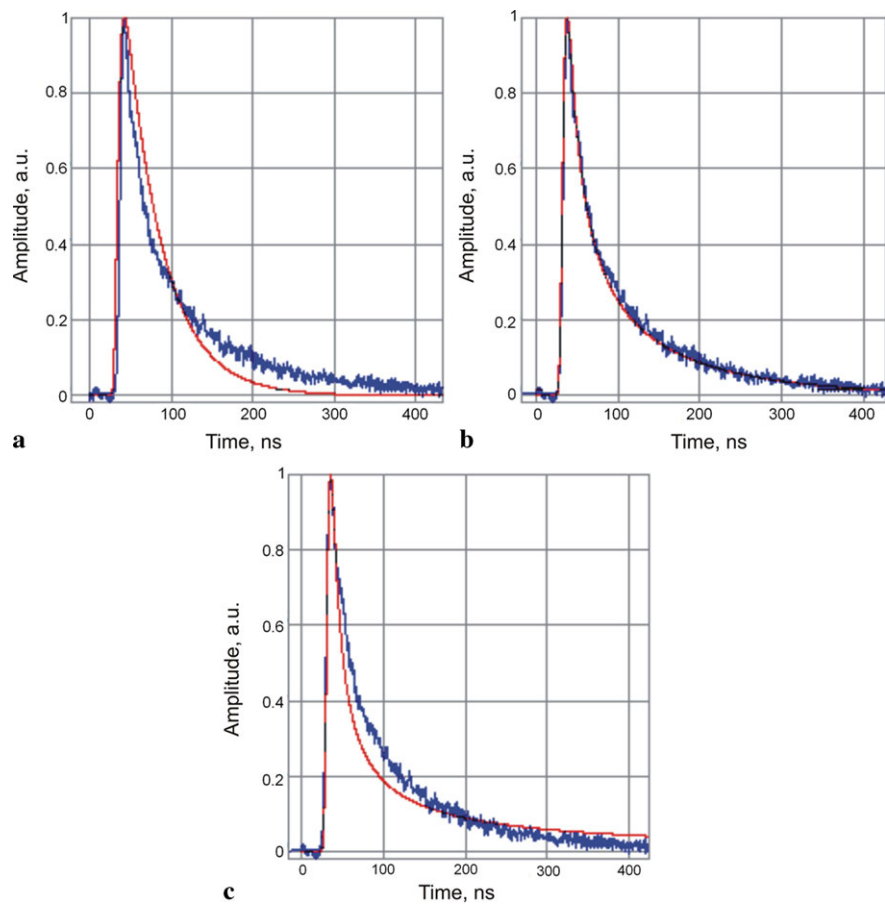


Fig. 13 Sensitivity analysis of particle CMD (a) and $E(m)$ (b), obtained by variation of model and experimental parameters

we would emphasize once again that the use of the obtained value of refractive index function in the model gave the best experimental LII signal approximation. The other higher or lower values of $E(m)$ set in the model lead to bad signal approximations and unrealistic iron particle sizes (see Fig. 12).

4.3 Uncertainties analysis

As we noted above, the main assumption at $E(m)$ size dependence analysis is the invariable particle density and heat capacity with the particle size. So the question is:

How could the variation of particle density and heat capacity during particle growth influence the $E(m)$ dependence on particle size? Variation of the assumed properties (density, heat capacity, accommodation coefficient, ratio of $E(m)_{760}/E(m)_{488}$ at registration wavelengths) and of the experimental conditions (gas temperature, pressure, laser fluence and particle heat up temperature measured by two-color pyrometry) lead to systematic errors of the measured values of CMD and $E(m)$. A detailed sensitivity analysis of these influences for carbon particles is given in Fig. 13, in terms of the percentages of changing of CMD and $E(m)$ with the variation of the above parameters. The results of an analysis of the sensitivity for iron particle were found to be close to carbon particles. The analysis of the results, presented in Fig. 13a, shows that the gas temperature, pressure, maximum particle temperature measured by two-color pyrometry and especially the ratio of $E(m)_{760}/E(m)_{488}$ supposed in LII model equal to 1 (see (9) and (10)), have a strong influence on the calculated value of CMD . Some of the parameters uncertainties lead to a canceling effect in the overall error. A detailed error calculation for all values including signal fitting (5%) results in an estimated overall uncertainty from -26% up to $+23\%$. An analysis of the influence of gas temperature, particle heat capacity, particle density, laser fluence, temperature measured by two-color pyrometry and ratio of $E(m)_{760}/E(m)_{488}$ on $E(m)$ value for carbon particles at wavelength of 1064 nm extracted from experiments is given in Fig. 13b. From Fig. 13b one can see that the maximum particle temperature, measured by two-color pyrometry and the ratio of $E(m)_{760}/E(m)_{488}$ have the main influence on the calculated value of $E(m)$. An error calculation for all values including fitting of two particle heat up temperatures (2%) described in Sect. 3.2 results in an estimated overall uncertainty in $E(m)$ determination between -34% and $+27\%$.

The next point is the sublimation/evaporation influence on the results obtained. In our model we used the properties of bulk graphite to account for the mass and heat loss by evaporation, described in Sect. 3.4. Usually mature soot particles could get a temperature of about 4000 K when evaporation takes place [35]. Our two-color measurements of heat up temperatures of nascent carbon and iron particles were found to be at 200–500 K less than the evaporation temperatures of bulk iron or carbon. So using the bulk properties, our evaporation sub-model does not show any essential influence on the results of the particle sizing. On the other hand the evaporation could play a role in our analysis, only if the particle evaporation temperature is lower than the one for bulk iron or graphite, respectively. However, to account for that we had to know the evaporation enthalpy and phase diagram for small particles, which are, unfortunately, not available (see [36]). So, only the rough estimation could be made that neglecting of evaporation will lead to an underestimation of measured particle sizes. The analysis of the influence

of probable evaporation on $E(m)$ values extraction could be the subject of future investigations.

5 Conclusions

The variation of carbon and iron nanoparticle optical properties during their growth was studied experimentally. For this goal the processes of carbon particle growth induced by shock wave pyrolysis of acetylene and iron particle formation after the laser pulse photolysis of iron pentacarbonyl were investigated. The application of two-color time-resolved laser-induced incandescence have allowed us to measure simultaneously the current particle size and refractive index function $E(m)$ at a wavelength of 1064 nm for the different stages of particle formation. It was found that increase of $E(m)$ of carbon and iron particles could be observed as particle size rises from 1–2 up to 15–20 nm. The results obtained are in an agreement with the observations of transparency of small particles (less than 5 nm) which one can often meet in the literature (see Sect. 1). Moreover, the values of $E(m)$ obtained for carbon particles with sizes of about 2–5 nm correspond to the UV data for visible-transparent carbon particles [34]. On the other hand, the values of $E(m)$ of the carbon particles with sizes of 14–20 nm tend to the well-known soot data [11, 23]. However, it should be pointed out that the quantity values of $E(m)$ presented in this work were extracted using rough assumptions about particle density, heat capacity and evaporation temperature taken to be independent on the particle size and taken from the bulk material data bases.

Acknowledgements This work is supported by RFBR and DFG.

References

1. R.L. Vander Wal, D.L. Dietrich, *Appl. Opt.* **34**, 1103 (1995)
2. T. Ni, J.A. Pinson, S. Gupta, R.J. Santoro, *Appl. Opt.* **34**, 7083 (1995)
3. D.R. Snelling, G.J. Smallwood, F. Liu, Ö.L. Gülder, W.D. Bachalo, *Appl. Opt.* **44**, 6773 (2005)
4. M.Y. Choi, K.A. Jensen, *Combust. Flame* **112**, 485 (1998)
5. H.A. Michelsen, *J. Chem. Phys.* **118**, 7012 (2003)
6. B.S. Haynes, H.Gg. Wagner, *Prog. Energy Combust. Sci.* **7**, 229 (1981)
7. S.C. Hendy, *Nanotechnology* **18**, 1 (2007)
8. F. Ding, K. Bolton, A. Rosen, *J. Vac. Sci. Technol. A* **22**, 1471 (2004)
9. F. Ding, K. Bolton, A. Rosen, *Phys. Rev. B* **70**, 075416-1 (2004)
10. V.N. Lihachev, T.Yu. Astahova, G.A. Vinogradov, M.I. Aliymov, *Russ. J. Phys. Chem. B* **26**, 89 (2007)
11. Ch. Schulz, B. Kock, M. Hofmann, H. Michelsen, S. Will, B. Bougie, R. Suntz, G. Smallwood, *Appl. Phys. B* **83**, 333 (2006)
12. P. Minutolo, G. Gambi, A. D'Alessio, *Proc. Combust. Inst.* **27**, 1461 (1998)
13. A. Emelianov, A. Eremin, H. Jander, H.Gg. Wagner, Ch. Borchers, *Proc. Combust. Inst.* **29**, 2351 (2002)

14. G. Basile, A. Rolando, A. D'Alessio, A. D'Anna, P. Minutolo, *Proc. Combust. Inst.* **29**, 2391 (2002)
15. A. D'Anna, A. Rolando, C. Allouis, P. Minutolo, A. D'Alessio, *Proc. Combust. Inst.* **30**, 1449 (2005)
16. H. Wang, *Proc. Combust. Inst.* **33**, 41 (2011)
17. H. Bladh, J. Johnsson, N.-E. Olofsson, A. Bohlin, P.-E. Bengtsson, *Proc. Combust. Inst.* **33**, 641 (2011)
18. R. Starke, B. Kock, P. Roth, *Shock Waves* **12**, 351 (2003)
19. D. Woiki, A. Giesen, P. Roth, *Proc. Combust. Inst.* **28**, 2531 (2000)
20. R. Starke, B. Kock, P. Roth, A. Eremin, E. Gurentsov, V. Shumova, V. Ziborov, *Combust. Flame* **132**, 77 (2003)
21. A.V. Eremin, E.V. Gurentsov, M. Hofmann, B. Kock, Ch. Schulz, *Appl. Phys. B* **83**, 449 (2006)
22. A.V. Eremin, E.V. Gurentsov, B. Kock, Ch. Schulz, *J. Phys. D, Appl. Phys.* **41**, 055203 (2008)
23. D. Snelling, F. Liu, G. Smallwood, Ö. Gülder, *Combust. Flame* **136**, 180 (2004)
24. M.W. Chase, C.A. Davies, J.R. Downey, D.J. Frurip, R.A. McDonald, A.N. Syverud, *J. Phys. Chem. Ref. Data* **14** (1985)
25. J.B. Austin, R.H.H. Pierce, *Phys., J. Gen. Appl. Phys.* **4**, 409 (1933)
26. W.W. Anderson, T.J. Ahrens, *J. Geophys. Res.* **99**, 4273 (1994)
27. B. Kock, C. Kayan, J. Knipping, H.R. Ortner, P. Roth, *Proc. Combust. Inst.* **30**, 1689 (2004)
28. F. Liu, K.J. Daun, D.R. Snelling, G.J. Smallwood, *Appl. Phys. B* **83**, 355 (2006)
29. H.A. Michelsen, F. Liu, B. Kock, H. Bladh, A. Boiarciuc, M. Charwath, T. Dreier, R. Hadeff, M. Hofmann, J. Reimann, S. Will, P.-E. Bengtsson, H. Bockhorn, F. Foucher, K.P. Geigle, C. Mounaim Rousselle, C. Schulz, R. Stirn, B. Tribalet, R. Suntz, *Appl. Phys. B* **87**, 503 (2007)
30. G.J. Smallwood, D.R. Snelling, F. Liu, Ö.L. Gülder, *Trans. ASME* **123**, 814 (2001)
31. H.R. Leider, O.H. Krikorian, D.A. Young, *Carbon* **11**, 555 (1973)
32. P. Roth, A.V. Filippov, *J. Aerosol Sci.* **27**, 95 (1996)
33. A.V. Filippov, M.W. Markus, P. Roth, *J. Aerosol Sci.* **30**, 71 (1999)
34. A. D'Alessio, A. D'Anna, P. Minutolo, L.A. Sgro, A. Violi, *Proc. Combust. Inst.* **28**, 2547 (2000)
35. S. De Iuliis, F. Migliorini, F. Cignoli, G. Zizak, *Appl. Phys. B* **83**, 397 (2006)
36. Q. Jiang, Z.P. Chen, *Carbon* **44**, 79 (2006)